Role of molybdenum in corrosion of iron-based alloys in contact with hydrogen sulfide containing solution

Georgi Genchev, Christoph Bosch, Elke Wanzenberg, Andreas Erbe*

Georgi Genchev

Max-Planck-Institut für Eisenforschung GmbH, 40237 Düsseldorf, Germany

Christoph Bosch

Salzgitter Mannesmann Forschung GmbH, Ehinger Str. 200, 47259 Duisburg, Germany

Elke Wanzenberg

Salzgitter Mannesmann Forschung GmbH, Ehinger Str. 200, 47259 Duisburg, Germany

Andreas Erbe

Max-Planck-Institut für Eisenforschung GmbH, 40237 Düsseldorf, Germany

Department of Materials Science and Engineering, NTNU, Norwegian University of Science and Technology, 7491 Trondheim, Norway

E-Mail a.erbe@mpie.de, aerbe@arcor.de

A sample iron molybdenum alloy with 3.4 wt.-% (2 at.-%) molybdenum, and pure iron, are exposed to hydrogen sulfide saturated saline solution for up to 56 d. In addition, their behaviour under anodic polarization in the same electrolyte is investigated. The initially fast dissolution of the iron molybdenum alloy slows down significantly over time, while iron cor-

rodes with a constant rate. The observed slow down of the corrosion rate can be described well with an exponential decay of the instantaneous corrosion rate with a time constant of (0.15 ± 0.03) d^{-1}, which implies stop in corrosion in practical terms after ≈2 w. Relationships are discussed between the instantaneous corrosion rate, and the time-averaged integral corrosion rate. Dissolution under anodic polarization of the iron molybdenum alloy is slower than for pure iron. While at certain times, pyrite, FeS_2, is found as corrosion product, the main corrosion product is mackinawite, FeS. The latter likely contains a certain fraction of molybdenum in case of the iron molybdenum alloy. On iron molybdenum, corrosion products forming a sealing layer are observed, which slow down further corrosion. The corrosion products on iron molybdenum show better adhesion to the base material surface.

Keywords: iron; molybdenum; polarization; sour gas; hydrogen sulfide; corrosion rate; integrated corrosion rate; weight loss; chloride

1 Introduction

Molybdenum is a metallic element commonly used as alloy element in steel and cast iron, as it enhances hardenability, strength, thoughness, and resistance to corrosion. The amount of molybdenum which can be alloyed in cast iron or iron-based materials is limited due to the precipitation of intermetallic phases, leading to embrittlement of the material. Detailed data about the thermodynamics of the iron-molybdenum system is available in the literature [1, 2]. Molybdenum is also an important component in stainless steels [3]. Molybdenum is known to provide excellent corrosion resistance in oxidizing environments under conditions of aqueous corrosion, as it participates in strengthening the passivating film formed on the surface, along with chromium and nickel. It is also important to note that already small amounts of molybdenum (≈2 wt.-%; all percentages in composition given here are wt.-% unless noted otherwise) led to a significant benefit [3]. With the help of anodic polarization

studies, molybdenum has been shown to have the particular benefit of raising the pitting potential [3].

Sulfide stress cracking (SSC) is observed when a material is exposed to the combined action of mechanical tensile stress and corrosion in the presence of aqueous hydrogen sulfide, H_2S. SSC is a form of hydrogen stress cracking and plays an important role in the gas and oil industry under conditions of sour service [4–6]. In this context, general principles for selection of cracking-resistant materials from the classes of carbon and low alloy steels, as well as cracking-resistant alloys (CRAs), are given in the NACE MR0175 (ISO 15156) [7].

SSC prevention was observed when molybdenum was added to a 13 % chromium steel [8]. Moreover, alloying of molybdenum, copper and nickel led to an overall better corrosion resistance towards carbon dioxide, CO_2, and hydrogen sulfide [8, 9]. Also for microalloyed steels, molybdenum was found to improve corrosion resistance [10–12] as a consequence of the formation of fine carbides during tempering [10, 13, 14]. For microalloyed steels with high sulfur content (≈0.025 %) resistance toward cracking increased with increasing molybdenum content. The highest resistance has been obtained with 0.3 % molybdenum [15, 16]. In case of high-strength, low-alloy steel, SSC resistance was also found to increase when 0.3 % molybdenum were added, both in combination with chromium and without chromium [17]. The observation was explained with a changes in the microstructure of the materials upon molybdenum addition. The modification of a standard steel by increasing the molybdenum amount to ≈0.75 % showed also superior high cycle fatigue resistance in hydrogen sulfide environment [18].

The corrosion of iron-molybdenum binary alloys up to 40 % was also studied in aqueous hydrogen sulfide solutions at high temperatures [19]. The corrosion rate decreased after molybdenum addition to iron. However, the reduction of the corrosion rate was reported to be independent of the molybdenum amount used [19]. The effect of alloyed molybdenum on the activation of anodic dissolution by reduced sulfur compounds have been investigated on iron-nickel-chromium-molybdenum alloys using electrochemical techniques [20]. Current studies

using iron-nickel-chromium-molybdenum alloys showed improved corrosion resistance, i.e. reduced stress corrosion cracking, SCC, and pitting corrosion, in the hydrogen sulfide/chloride environment due to the addition of molybdenum [21]. The authors discussed the possible mechanism on the basis of a reductive desorption: sulfur, S^0, bridging molybdenum atoms is unstable and reduced to hydrogen sulfide. The same mechanism was used to explain the higher passivation current densities of 316L stainless steel compared to 304L obtained from potentiodynamic measurements in sulfide-containing electrolytes [22]. An extended review of literature and experience on the roles of hydrogen sulfide in the behavior of engineering alloys is given by [23].

When the molybdenum content added to an iron-based alloy increases above a certain threshold, ferrite is formed, which has a negative effect on the SSC resistance [3, 24].

In this work, the corrosion of a binary iron molybdenum alloy with 3.4 % molybdenum was investigated in hydrogen sulfide saturated aqueous solutions by comparing mass loss and electrochemical data. The comparison between mass loss and electrochemical measurements was motivated by the fact that a binary alloy may dissolve by dealloying, leading to enrichment of one component near the surface in the process [25]. In nickel-base alloys, dealloying of molybdenum has been found to be the decisive corrosion mechanism under certain conditions [26–28]. However, the situation is reversed in iron-based alloys: molybdenum is slightly more noble than iron [29, 30], but the differences are small, so that it is not clear if significant differences in dissolution rate and consequent enrichment of molybdenum are to be expected [25]. On stainless steels, iron and molybdenum have been found to dissolve together, leaving copper behind [31]. Also under active-passive transitions of stainless steels, no special role of molybdenum was found [32]. An enrichment of one component makes electrochemical data hard to interpret without detailed surface characterisation. Corrosion products where consequently analysed by scanning electron microscopy (SEM), X-ray diffraction (XRD) and Raman spectroscopy. The detailed characterisation led to a suggested explanation for the improvement in corrosion resistance of iron due to the addition of molybdenum.

2 Materials and methods

2.1 Materials

A binary iron alloy containing 3.4 % of molybdenum (referred to as FeMo in this work) was prepared in house by standard metallurgical processes. Alloys were used as prepared, i.e. without dedicated thermal or mechanical postprocessing. The content of carbon was ≈0.0023 %. As comparison, Armco iron was used.

Both iron and molybdenum have a bcc structure with molybdenum having an atomic radius of 1.40 Å (iron: 1.26 Å) [33]. A symmetric XRD θ-2θ scan in the range of 10° – 75° of 2θ showed a shift in the reflections of the collected patterns for the binary alloy compared to database values for pure iron. The position of the reflections point to the presence of a structure where molybdenum atoms are replacing iron atoms in a bcc lattice. The data was fitted using Maud (http://maud.radiographema.com/) using the 110 and 200 reflections. The bigger molybdenum atoms lead to expansion of the lattice [for iron, lattice constant a = 2.8695(6) Å, while in the FeMo binary alloy a = 2.8760(4) Å].

2.2 Electrochemical and corrosion experiments

For free corrosion experiments, samples were ground with 320 SiC grinding paper, cleaned, and placed inside a PTFE holder. The holder, including the samples, was placed in a glass vessel with an overall volume of 3 L. The area exposed to electrolyte was ≈8.8 cm^2. NACE A standard solution was used as electrolyte (5 wt.-% sodium chloride, and 0.5 wt.-% acetic acid) [5]. Chemicals were obtained from Merck and used as received. Ultrapure water for solution was used from a USF ELGA Purelab Plus UV water purification system (Ransbach-Baumbach, Germany). Solutions were de-oxygenated for at least 1 h prior to experiments by purging with nitrogen. Subsequently, the solutions were purged for 1 h with hydrogen sulfide gas (1 bar). Titration with thiosulfate and starch solution after addition of iodine to the hydrogen sulfide purged solution was used to determine the amount of hydrogen sulfide

in solution. Hydrogen sulfide content was determined once before and once after the end of exposure of the samples. The pH of the solution was also measured during experiments. Hydrogen sulfide purge was maintained throughout the experiments to ensure a constant hydrogen sulfide concentration and minimize ingress of oxygen. Samples were exposed to the solution for exposure times of 96, 168, 336, 672, and 1344 h (4 d, 7 d=1 w, 14 d=2 w, 28 d=4 w and 56 d=8 w).

After the end of exposure, samples used for further analyses (SEM, XRD, Raman) were washed with distilled water and placed in a chamber with continuous nitrogen purge to dry. Samples used for determining mass loss were weighed before exposure to determine the mass at time t=0. After exposure, samples were dipped in inhibited hydrochloric acid (10 wt.-% of hexamethylenetetramine in 2M hydrochloric acid). Residues of corrosion products were also removed mechanically using a soft brush. After removing the corrosion products, the samples were weighed again. From the difference in weight, mass loss W for the different samples was determined. This mass loss was used to calculate time-averaged integrated corrosion rates $CR(t)$ up to the time t of exposure as $CR(t) = W/\rho A t$. Using W in mg, metal density ρ in g cm^{-3}, sample area A in cm^2, and exposure time t in h, with the conversion factor 8760 h a^{-1} $\cdot$ 10^{-2} yields

$$CR(t) = 8760 \left[\frac{\mathrm{h}}{\mathrm{a}}\right] \cdot 10^{-2} \cdot \frac{W}{\rho \cdot A \cdot t}, \tag{1}$$

$CR(t)$ in mm per year, mm a^{-1}. It is worth noting that $CR(t)$ is related to the instantaneous corrosion rate $r(t)$ as would be measured e.g. in a linear sweep voltametry (LSV) experiment by

$$CR(t) = \frac{1}{t} \int_0^t r(t')\mathrm{d}t'. \tag{2}$$

For the electrochemical experiments, including a determination of the polarization resistance R_p of layers formed by free corrosion, a three electrode setup was used, with a carbon rod (Mueller and Roessner, Troisdorf, Germany) as counter electrode, a commercial Ag/AgCl/3M KCl (Metrohm, Filderstadt, Germany) in a Luggin capillary as reference elec-

trode, and the sample of interest as working electrode. The setup consisted of a home-built air-tight PMMA cell with area of exposure for the sample of 0.785 cm^2, and an electrolyte volume of 500 mL. For such experiments, purging with nitrogen and subsequently with hydrogen sulfide was performed for approximately 30 min each. As a potentiostat a Gamry PCIV/Series G Family (Gamry Instruments) or a PGU 1A-OEM was used.

Potentiostatic polarization experiments were conducted at potentials positive of the corrosion potential E_{corr}, +200 mV above E_{corr}. LSV was used to investigate products from free corrosion experiments. For LSV, a potential range of ±30 mV around E_{corr} and scan rate of 0.1667 mV s^{-1} were used. When investigating corrosion products formed by potentiostatic polarization, a potential range of ±120 mV around E_{corr} and a scan rate of 1 mV s^{-1} were used. Kinetic parameters have been extracted using the Stern Geary analysis [34].

All experiments were carried out with three repeats.

2.3 Characterization

The resulting surface morphology was observed using a Zeiss Leo Gemini 1550 scanning electron microscope (SEM; Carl Zeiss NTS GmbH, Oberkochen, Germany) with energy (EHT) of 10 kV. In this work, energy dispersive X-ray spectroscopy (EDS) was not reasonable to use as an analysis method, because molybdenum and sulfur show EDS lines at similar energies and are consequently hard to distinguish.

Grazing incidence XRD experiments were performed on a Bruker D8 Advance diffractometer with Cu K_α radiation and a Sol-X solid state detector. The diffraction patterns have been collected at an angle of incidence $\alpha = 3°$ within a range of the scattering angle 2θ of $10° < 2\theta < 75°$ in steps of 0.05°, with an integration time of 60 s per step. Resulting patterns were evaluated using the DIFFRACplus EVA package. Exact peak positions for fine analysis where determined by fitting the respective diffraction peak with a single Gaussian peak function and using its maximum.

For the identification of the corrosion products via Raman spectroscopy, an alpha300M

(WITec, Ulm, Germany) confocal Raman microscope was used, with an excitation wavelength of 532.1 nm. Illumination and detection was performed through a microscope objective of 100×, numerical aperture 0.75. Details on the stabilisation of the corrosion products against oxidation are available elsewhere [35].

A cross-section of the surface with sulfide layer has been prepared using a FEI Helios Nanolab 600i dual-beam FIB/SEM instrument.

3 Results

Both free corrosion experiments as well as potentiostatic polarization experiments led to the formation of black precipitates on the metal surface. In some cases, LSV scans have been additionally conducted before and after film formation, from which polarization resistance R_p, E_corr and other electrochemical parameters were calculated. However, performing LSV on a bare metal prior to free corrosion experiments could lead to changes in the surface properties and the formation of different corrosion products during the process.

3.1 Free corrosion experiments

Long-term exposure under regular monitoring of the concentration of hydrogen sulfide and pH have been conducted for pure iron and FeMo samples. In all experiments, the hydrogen sulfide concentration was in the range of 2300 – 2800 ppm; the pH was increasing during the experiments and reached a final value of ≈3.8. The initial pH of the electrolyte was 2.6, which increased to 2.9 after hydrogen sulfide saturation before sample exposure. SEM micrographs show the progress in the film formation of the corrosion products (Fig. 1 and Fig. 2). Non-uniform coverage of the surface in the beginning, some blistering effects (7 d) and formation of huge crystals of iron sulfides (after 28 d) are features observed for the pure iron samples. XRD data indicates the presence of mostly mackinawite as crystalline phase, but a small amount of pyrite was detected in the initial phase of the corrosion process (Fig. 1f). The FeMo sample

showed different morphologies, forming a dense layer of corrosion products on the surface already after 7 d. With increasing time, cracks developed after drying. Consequently, part of the corrosion products spalled off the surface. For FeMo, mackinawite was found to be the main corrosion product. Pyrite was also present, but its amount was decreasing with increasing reaction time. After 28 d, no pyrite was detected any more (Fig. 2f).

CR is plotted versus time in Fig. 3. CR around (0.4 ± 0.05) mm a^{-1} were detected in the case of pure iron throughout the experiments. A much higher CR was initially observed for the FeMo alloy. However, CR rapidly decreased with time, leading to lower values of 0.2 – 0.3 mm a^{-1} compared to pure iron after longer exposure times (28 and 56 d). This shall be discussed in detail in section 4.1.

A FIB cross section of the corrosion product layer formed after 28 d on a FeMo substrate is shown as inset in Fig. 3. A corrosion product layer with an overall thickness of ≈50 μm was observed. The inner part, ≈35 μm in thickness, was very porous, while the top ≈12 – 13 μm layer was dense.

In separate experiments, R_p of layers grown for 7 d under the same conditions was determined using data from LSV measurements. The value in case of pure iron was significantly higher [(336 ± 35) Ω cm^2] than the one of the FeMo alloy [(121 ± 6) Ω cm^2], but the order of magnitude is the same. Also a significant decrease in E_{corr} was observed for pure iron, while the value did not change for FeMo (see Fig. 4). A comparison of the Tafel plots of both materials show higher anodic and cathodic current densities for the layer formed on the FeMo substrate (Fig. 4).

3.2 Potentiostatic growth of corrosion products

Potentiostatic polarization was used in this work to enhance anodic metal dissolution and thus increase speed of formation of corrosion products. As shown previously for pure iron, no passivation of a surface was reached using this method [36], because the formed films are spalling off the substrate allowing the formation of further corrosion products. Typi-

cal transients from potentiostatic polarization experiments at potentials above E_{corr} and the corresponding current densities over time for the materials of interest are shown Fig. 5. Results showed much lower current densities over time when molybdenum was present (Fig. 5a). Moreover, the mass losses after the experiments were significantly lower when polarizing FeMo instead of pure iron (Fig. 5a inset). Fig. 5b and c represent the results of LSV measurements for both materials before and after a layer of corrosion products has been synthesized using potentiostatic polarization. The Tafel plots show similarities, pointing to similar properties of the electrochemically formed layers, which were not significantly influenced by the presence of molybdenum. However, cathodic currents were much higher when corrosion products were synthesized on a FeMo binary alloy, indicating higher amounts of hydrogen being produced during the process. Electrochemical parameters (E_{corr}, corrosion current density i_{corr}, cathodic β_c and anodic β_a Tafel slopes, and R_{p}) determined from the experiments are compiled in Tab. 1.

The corrosion products formed after potentiostatic polarization on FeMo were black in colour and possessed a morphology which is similar to the one observed after 4 d of free corrosion. Plate-like crystals with gaps between each other covered the surface (Fig. 6). The thickness of the layer was determined to be $\approx$7 μm. Raman spectra of dried corrosion products always transform to hematite as a consequence of laser light heating in the presence of oxygen [35]. Fig. 6d shows a Raman spectrum of the corrosion products formed on the FeMo surface when the sample is still covered by a thin water layer during the measurements, protecting the sample from possible transformation due to laser heating [35]. Some minor beam damage was observed after longer exposure times, as shown in the inset of the Raman spectrum. Two sharp Raman bands were detected in the measurements at at 209 cm^{-1} and 290 cm^{-1} (shoulder). The bands are similar in position to those observed on bare iron and discussed in detail elsewhere [35]. These bands are seen as an indication of microcrystalline mackinawite [37–39]. The XRD pattern of the corrosion products also pointed to the formation of mackinawite (FeS), which has been also observed for the pure iron sample

[36]. In this case, a 0.05° 2θ shift in the position of the main 001 reflection of mackinawite (ICCD nr. 01-086-0389) was observed, corresponding to an expansion of the crystal lattice by 0.016 Å. Additionally, reflections arising from sodium chloride impurities and the metal substrate ($Fe_{0.97}Mo_{0.03}$, ICCD nr. 03-065-7296) were observed.

4 Discussion

4.1 Free corrosion experiments

This discussion shall start with the corrosion rates. It is worth noting that due to the nature of the measurement of CR, initially high values will continue to affect the values at later stages (compare eq. 1 and 2). Therefore, CR can never reach 0, even if corrosion was to stop completely. If after 7 d for the FeMo sample corrosion was to cease, CR after 28 d would be $\approx$0.18 mm a^{-1}, and after 56 d $\approx$0.1 mm a^{-1}. The actually determined CR remains slightly above these values. So, let us quantitatively discuss the relationship between the integral corrosion rate $CR(t)$ which determines mass loss and the total amount of formed corrosion products, and the instantaneous corrosion rate $r(t)$ which determines how much material transforms at a certain time. The latter quantity would determine i_{corr} and also affect E_{corr}. Table 2 shows how different instantaneous corrosion rates $r(t)$ transform into time-averaged integral corrosion rates $CR(t)$.

A constant corrosion at all times would obviously lead also to a constant integral corrosion rate (example 1 in Table 2). If corrosion stops completely after a certain time t_0 (example 2 in Table 2), $CR(t)$ will decay with $1/t$. A similar decay is observed if there is an exponential decay with a reciprocal time constant κ^{-1} short compared to the duration of the experiment (limit for large t in example 4 in Table 2). A power law decay in $r(t)$ will lead to a power law decay in $CR(t)$ with the same exponent (example 3 in Table 2). If an exponential decay in $r(t)$ is observed with a reciprocal time constant κ^{-1} on the order the duration of the experiment(s), a slightly more involved functional shape is obtained (example 4 in Table 2).

SEM images show a growth of corrosion products on the materials surface after longer exposure in free corrosion experiments. Likewise, the corrosion products became more prominent in the XRD analysis. On pure iron, the corrosion rates [both $r(t)$ and $CR(t)$] were constant. On FeMo, $CR(t)$ [and consequently also $r(t)$] was initially much higher than on iron, however, a significant drop in $r(t)$ must have occurred on FeMo, leading to the observed reduction in $CR(t)$.

The electrochemical measurements after 7 d of free corrosion show that R_p on pure iron is almost three times as high compared to FeMo. Because $r(t) \propto i_{\mathrm{corr}} \propto 1/R_p$, $r(t)$ after 7 d of exposure is still higher on FeMo than on iron. Consequently, the main drop in corrosion rate must therefore occur after that time. For more quantitative information, the data for $CR(t)$ displayed in Fig. 3 was fitted to the different models relating $r(t)$ to $CR(t)$ shown in Table 2. The results of fitting are shown in Fig. 7. First, the data were analysed on a double logarithmic scale to verify if a simple power law of the form $CR \propto t^{-\kappa}$ would be observed (Fig. 7a). The result is a mediocre fit, where an exponent $\kappa = (0.66 \pm 0.09)$ was obtained. This result rules out the second model of Table 2. Overall, however, the curve looks to be of more complex shape than represented by such a model. It needs to be stressed that both time range and range in CR are on the lower limit to be suitable for this analysis, as both of them span approximately one order of magnitude only.

Fitting the observed data to an exponential decay in $r(t)$, i.e.

$$CR(t) = \frac{A}{\kappa t}\left(1 - \mathrm{e}^{-\kappa t}\right), \tag{3}$$

results in the fit shown as solid line in Fig. 7b, which describes the observed data sufficiently well. The extracted parameters were $\kappa = (0.15 \pm 0.03)$ d^{-1} and $A = (1.2 \pm 0.2)$ mm a^{-1}. With these parameters, the curve for $r(t)$ was calculated and added to Fig. 7b as dotted line, which is compared to the constant corrosion rate in iron. This line shows that after almost 10 d, $r(t)$ decays to a level reached for iron. After 30 – 40 d, $r(t)$ reaches values below 0.01 mm a^{-1}, which in practical terms are quite low.

A possible explanation for the observed drop in corrosion rate for FeMo is the formation of a protective corrosion product. Fig. 2 shows a homogeneous coverage of the surface with corrosion products. The inset of Fig. 3 shows a cross section through such a corrosion product layer on FeMo, with a dense outer and a porous inner layer. The layers will in any case become a barrier for mass transfer. On the other hand, no protective corrosion products were observed on pure iron: significant amounts of corrosion products spall off the surface. These products were not detected in the final surface analysis.

XRD patterns show that in the experiments under conditions of free corrosion, the iron sulfide pyrite, FeS_2, was a prominent corrosion product, especially in the initial stages. Later, the iron sulfide mackinawite, FeS, became the dominating corrosion product. This is different from previous observations, where nanocrystalline mackinawite was already identified as the initial corrosion product after much shorter exposure times than the shortest used here [36, 40]. Overall, an initial, possibly nanocrystalline mackinawite then typically recrystallises to form crystalline mackinawite [35, 37, 38]. A thermodynamic analysis of the system showed that pyrite is the expected, thermodynamically stable corrosion product in certain ranges of the predominance diagram [36], in general at higher electrode potentials and lower pH compared to mackinawite. A reduction of pyrite according to

$$FeS_2 + H_2 \longrightarrow FeS + H_2S \tag{4}$$

by hydrogen formed in the sour gas corrosion process is also possible. It is furthermore possible that an already formed layer of pyrite is covered by freshly forming mackinawite, which is then set to determine the XRD signal.

4.2 Potentiostatic polarization experiments

Anodic polarization enhances the dissolution reaction, and should hence speed up the overall disintegration of the material; it can be seen as a model for the processes in the anodic

region of the freely corroding surface. Current densities in the chronoamperometric measurements during potentiostatic polarization decreased to roughly one half by introduction of molybdenum, which indicates a slow-down in dissolution rate. The comparison can be made quantitatively. The chronoamperometry data can be used to obtained average dissolution current densities of 7300 µA cm^{-2} on iron, and 4200 µA cm^{-2} on FeMo. Using

$$W = \frac{iMA}{zF}t \tag{5}$$

with molar mass M of iron, Faraday constant F and valency $z = 2$ yielded expected mass loss from electrochemical data. After polarisation times of 2 h and 6 h, mass losses of 12 mg and 36 mg, respectively, were calculated for iron, and 7 mg and 21 mg, respectively, for FeMo. These values agree well with experimentally determined mass losses. The measured mass loss was lower for FeMo compared to iron, by about the amount expected from the current densities.

While the dissolution rate was lower for FeMo, the dissolution was constant after an initial phase of decrease, and did not decrease further, i.e. no passivation of the surface was observed. An overall constant dissolution rate is furthermore a hint to a constant composition of the surface region: if the composition was changing significantly, the dissolution rate should also change.

The Tafel plots on both iron and FeMo after polarization were quite similar, indicating that the main anodic and cathodic processes occur in a similar fashion on iron and FeMo. The cathodic branch showed an increased current density after potentiostatic polarization, indicating a higher activity for hydrogen evolution. The corrosion products on FeMo may hence have more active sites for hydrogen evolution. SEM micrographs of the corrosion products on FeMo after potentiostatic polarization for 6 h showed similarities to the corrosion products observed after 4 d of exposure under free corrosion conditions.

The XRD pattern showed a shift in the position of the 001 reflection of the mackinawite corrosion product, even though the position of the 001 reflection of mackinawite has been

found in previous studies of the authors to be quite stable [36]. This shift may be caused by the slightly larger molybdenum atom replacing iron atoms in the FeS mackinawite lattice, so that the corrosion product is actually an molybdenum-doped mackinawite. Such a corrosion product may form directly from the substrate, which shows a phase with some molybdenum in the iron lattice as well. XRD and Raman spectroscopy show no evidence for the presence of a corrosion product of pure molybdenum, e.g. MoS_2 or Mo_2S_3. The Raman spectra show no peak at 1300 cm^{-1}, indicating that no oxidation of the corrosion products took place [35].

5 Summary and conclusions

Initially, the FeMo alloy corroded fast in free corrosion experiments, but dissolution stopped almost completely after ≈2 w. Under potentiostatic polarization, the FeMo alloy dissolved also slower than pure iron. An analysis of the corrosion products shows that after longer exposures, the FeMo alloy formed a dense layer at the surface, which is obviously beneficial for slowing down dissolution. There is some evidence that the mainly mackinawite-based corrosion products in case of the FeMo alloy contain molybdenum, possibly replacing iron atoms. Likewise, there is no evidence for the formation of corrosion products containing purely molybdenum sulfides. The corrosion products observed here are likely also metallic in nature [36], which implies that they do not act as an efficient barrier for charge transport. On FeMo, the corrosion products adhere better to the surface than on pure iron. Consequently, lattice strain between base material and corrosion product is lowered by the presence of molybdenum, which is likely the main reason for the observed lower corrosion rates in the presence of molybdenum.

Acknowledgements

The authors thank Hauke Springer for helpful discussions. A.E. and G.G. thank Salzgitter

Mannesmann Forschung GmbH for funding a collaborative research project.

6 References

1. A. Guillermet, *Bull. Alloy Phase Diagrams* **1982**, *3*, 359.

2. B. Predel, in O. Madelung (Ed.), *Dy-Er – Fr-Mo*, *Landolt-Börnstein - Group IV Physical Chemistry*, vol. 5e, Springer Berlin Heidelberg **1995**, 1–5.

3. P. A. Schweitzer, *Corrosion Engineering Handbook, 2nd edition*, CRC Press, Boca Raton, USA **2006**.

4. *NACE Standard MR0103: Materials Resistant to Sulfide Stress Cracking in Corrosive Petroleum Refining Environments*, NACE International, Houston, Texas, USA **2012**.

5. *NACE Standard TM0177-2005: Laboratory Testing of Metals for Resistance to Sulfide Stress Cracking and Stress Corrosion Cracking in H_2S Environments*, NACE International, Houston, Texas, USA **2005**.

6. *NACE Standard TM0284-2003: Evaluation of Pipeline and Pressure Vessel Steels for Resistance to Hydrogen-Induced Cracking*, NACE International, Houston, Texas, USA **2003**.

7. *NACE Standard MR0175 / ISO15156: Petroleum and Natural Gas Industries - Materials for Use in H_2S-containing Environments in Oil and Gas Production*, International Organization for Standardization (ISO) / American National Standards Institute (ANSI) / NACE International, Geneva, Switzerland / New York, New York, USA / Houston, Texas, USA **2001**.

8. H. Asahi, A. Kawakami, A. Takahashi, N. Sato, T. Hara, M. Sugiyama, S. Sakamoto, G. Shigesato, *Nippon Steel Tech. Rep. Japan* **1997**, *72*, 7.

9. K. Ravi, V. Ramaswamy, T. Namboodhiri, *Mater. Sci. Eng. A* **1990**, *129*, 87.

10. P. Grobner, D. Sponseller, D. Diesburg, *Corrosion* **1979**, *35*, 240.

11. Y. Yoshino, *Corrosion* **1982**, *38*, 156.

12. M. D. Tumuluru, *Mater. Perform.* **1987**, *26*, 9.

13. B. D. Craig, *Metall. Mater. Trans. A* **1982**, *13*, 1099.

14. M. Tanimura, Y. Ishizawa, T. Shimada, *Nippon Kokan Tech. Rep. Overseas* **1983**, 42.

15. K. Ravi, V. Ramaswamy, T. Namboodhiri, *Mater. Sci. Eng. A* **1993**, *169*, 111.

16. C.-M. Liao, J.-L. Lee, *Corrosion* **1994**, *50*, 695.

17. S. Koh, J. Lee, B. Yang, K. Kim, *Corrosion* **2007**, *63*, 220.

18. K. Tsukada, K. Minakawa, A. McEvily, *Metall. Trans. A* **1983**, *14*, 1737.

19. W. Kai, D. Douglass, F. Gesmundo, *Oxid. Met.* **1992**, *37*, 389.

20. A. Betts, R. Newman, *Corros. Sci.* **1993**, *34*, 1551.

21. A. Tomio, M. Sagara, T. Doi, H. Amaya, N. Otsuka, T. Kudo, *Corros. Sci.* **2015**, *98*, 391 .

22. A. Davoodi, M. Pakshir, M. Babaiee, G. Ebrahimi, *Corros. Sci.* **2011**, *53*, 399.

23. R. Kane, M. Cayard, *NACE: Int. Corros. Conf. Ser.* **1998**, 274.

24. T. Hara, H. Asahi, *CAMP-ISIJ* **1996**, *9*, 1392.

25. H. Kaiser, G. A. Eckstein, *Encyclopedia of Electrochemistry*, Wiley-VCH, Weinheim, Germany, vol. 4, chap. Corrosion of Alloys **2007**, 156–186.

26. N. Boukis, W. Habicht, E. Hauer, K. Weiss, E. Dinjus, in *EUROCORR 2008 - European Corrosion Congress: Managing Corrosion for Sustainability, Book of Abstracts*, European Federation of Corrosion, DECHEMA e.V., Frankfurt(Main), Germany, 169.

27. W. Habicht, N. Boukis, E. Hauer, E. Dinjus, *X-Ray Spectrom.* **2011**, *40*, 69.

28. H. Kim, D. B. Mitton, R. M. Latanision, *J. Electrochem. Soc.* **2010**, *157*, C194.

29. B. Beverskog, I. Puigdomenech, *Corros. Sci.* **1996**, *38*, 2121.

30. M. Pourbaix, *Atlas of Electrochemical Equilibria in Aqueous Solutions*, National Association of Corrosion Engineers / Centre Belge d'Etude de la Corrosion CEBELCOR, Houston / Bruxelles **1974**.

31. K. Ogle, J. Baeyens, J. Swiatowska, P. Volovitch, *Electrochim. Acta* **2009**, *54*, 5163 .

32. K. Ogle, M. Mokaddem, P. Volovitch, *Electrochim. Acta* **2010**, *55*, 913 .

33. E. Wiberg, N. Wiberg, *Hollemann Wiberg: Lehrbuch der Anorganischen Chemie, 102nd ed.*, Walter de Gruyter, Berlin **2007**.

34. M. Stern, A. L. Geary, *J. Electrochem. Soc.* **1957**, *104*, 56.

35. G. Genchev, A. Erbe, *J. Electrochem. Soc.* **2016**, *163*, C333.

36. G. Genchev, K. Cox, T. H. Tran, A. Sarfraz, C. Bosch, M. Spiegel, A. Erbe, *Corros. Sci.* **2015**, *98*, 725 .

37. J. A. Bourdoiseau, M. Jeannin, R. Sabot, C. Rmazeilles, P. Refait, *Corros. Sci.* **2008**, *50*, 3247.

38. Y. El Mendili, B. Minisini, A. Abdelouas, J.-F. Bardeau, *RSC Adv.* **2014**, *4*, 25827.

39. M. Langumier, R. Sabot, R. Obame-Ndong, M. Jeannin, S. Sablé, P. Refait, *Corros. Sci.* **2009**, *51*, 2694 .

40. D. W. Shoesmith, M. G. Bailey, B. Ikeda, *Electrochim. Acta* **1978**, *23*, 1329.

Graphical abstract

Molybdenum has been used to reduce the susceptibility of certain steels to sour gas corrosion, i.e. corrosion in hydrogen sulfide, H_2S, containing environments. This work uses a model alloy to show that addition of molybdenum stops the dissolution of iron almost completely under sour gas conditions.

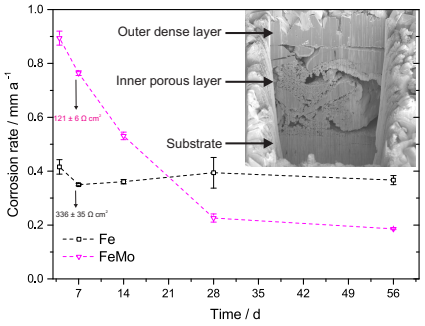

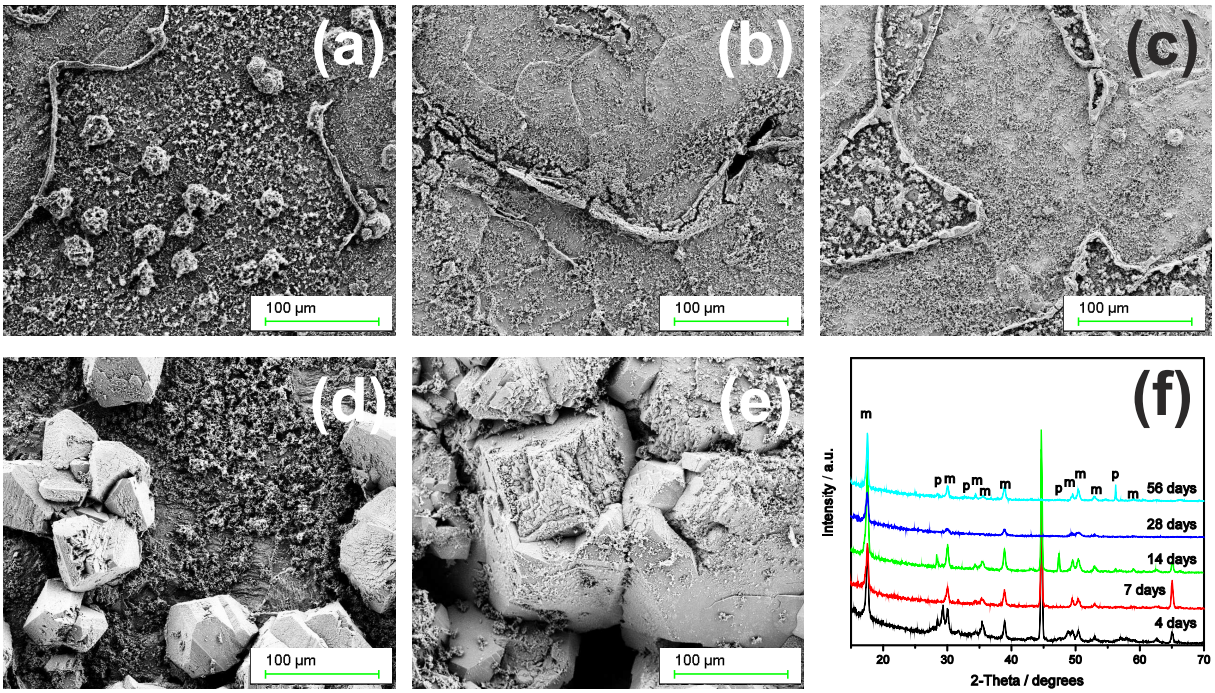

Figure 1: SEM micrographs showing the coverage with corrosion products of the pure iron surface after (a) 4 d (96 h), (b) 7 d (168 h), (c) 14 d (336 h), (d) 28 d (672 h), and (e) 56 d (1344 h) of exposure to the hydrogen sulfide saturated electrolyte. (f) XRD patterns of the corrosion products showing FeS (mackinawite, m) as the main corrosion product, and minor amounts of FeS_2 (pyrite, p). The reflection at 45° 2θ arose from the used metal substrate.

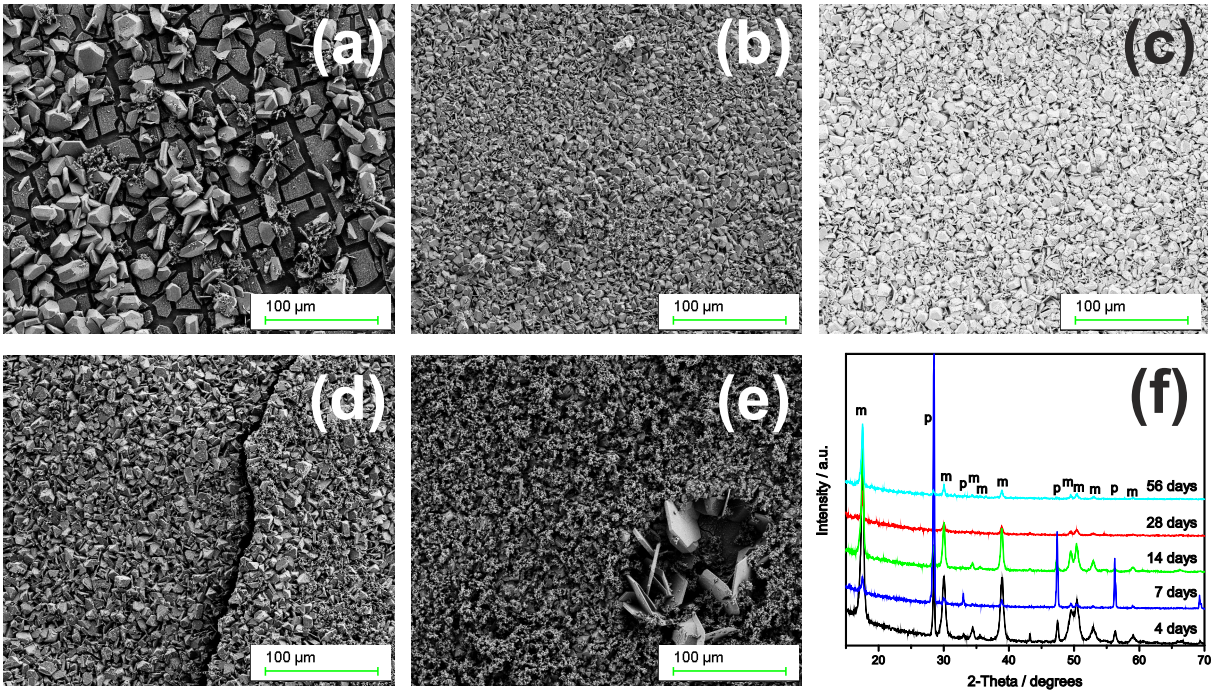

Figure 2: SEM micrographs showing the coverage with corrosion products of the FeMo binary alloy surface after (a) 4 d (96 h), (b) 7 d (168 h), (c) 14 d (336 h), (d) 28 d (672 h), and (e) 56 d (1344 h) of exposure to the hydrogen sulfide saturated electrolyte. (f) XRD patterns of the corrosion products showing the presence of FeS_2 (pyrite, p) and FeS (mackinawite, m) with changing ratio over time.

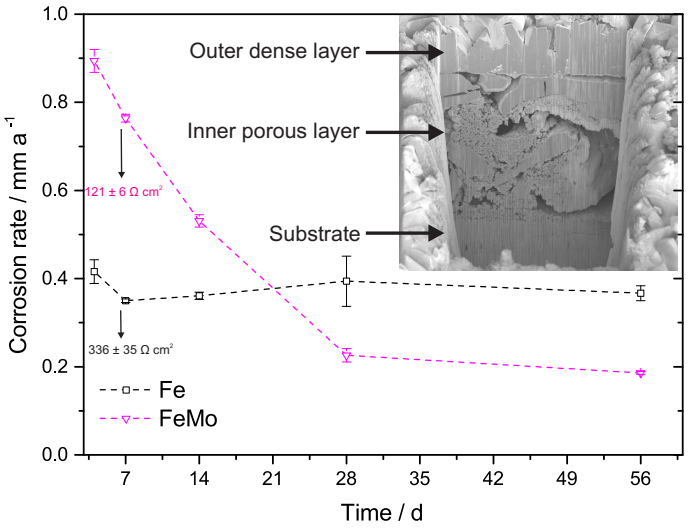

Figure 3: Time-averaged integrated corrosion rates $CR(t)$ calculated using eq. 1 from mass loss data for samples corroding under conditions of free corrosion. R_p extracted from LSV measurements (see Fig. 4) for a reaction time of 7 d (168 h) are indicated as numbers. The inset shows a side view of a cross-section prepared from a FeMo sample after 28 d (672 h) of exposure to a hydrogen sulfide saturated saline solution.

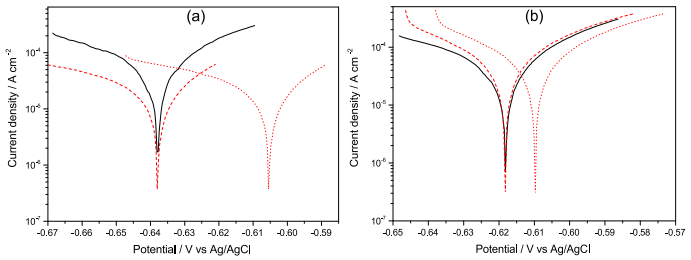

Figure 4: Tafel plots from LSV experiments for (a) pure iron and (b) FeMo binary alloy. Straight (dotted) curves represent measurements without (with) layer of black corrosion products obtained after 7 d of free corrosion. A shift on the potential axis of the dotted curves (dashed lines) serves for better visualization of the differences before and after film formation.

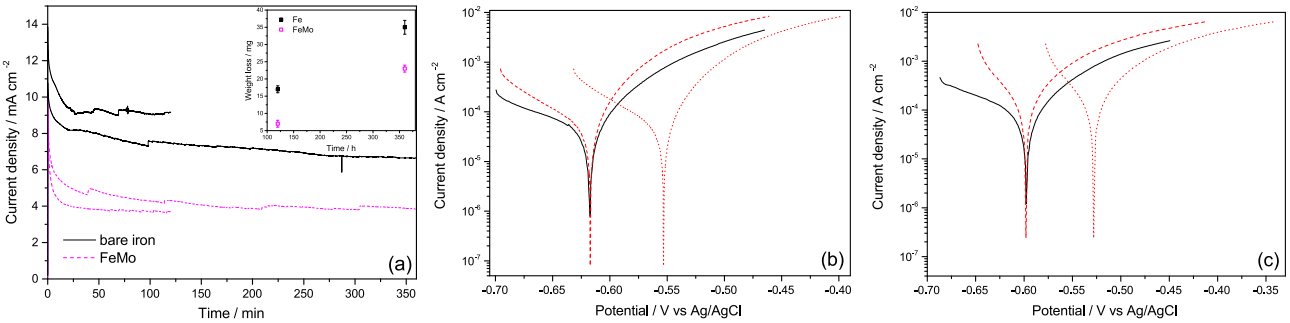

Figure 5: (a) Chronoamperometric transients from potentiostatic polarization experiments at 200 mV above initial E_{corr}. Inset: mass loss after polarization. (b) and (c) show the Tafel plots extracted from LSV measurements for pure iron and FeMo, respectively. Lines correspond to the same samples as indicated in Fig. 4.

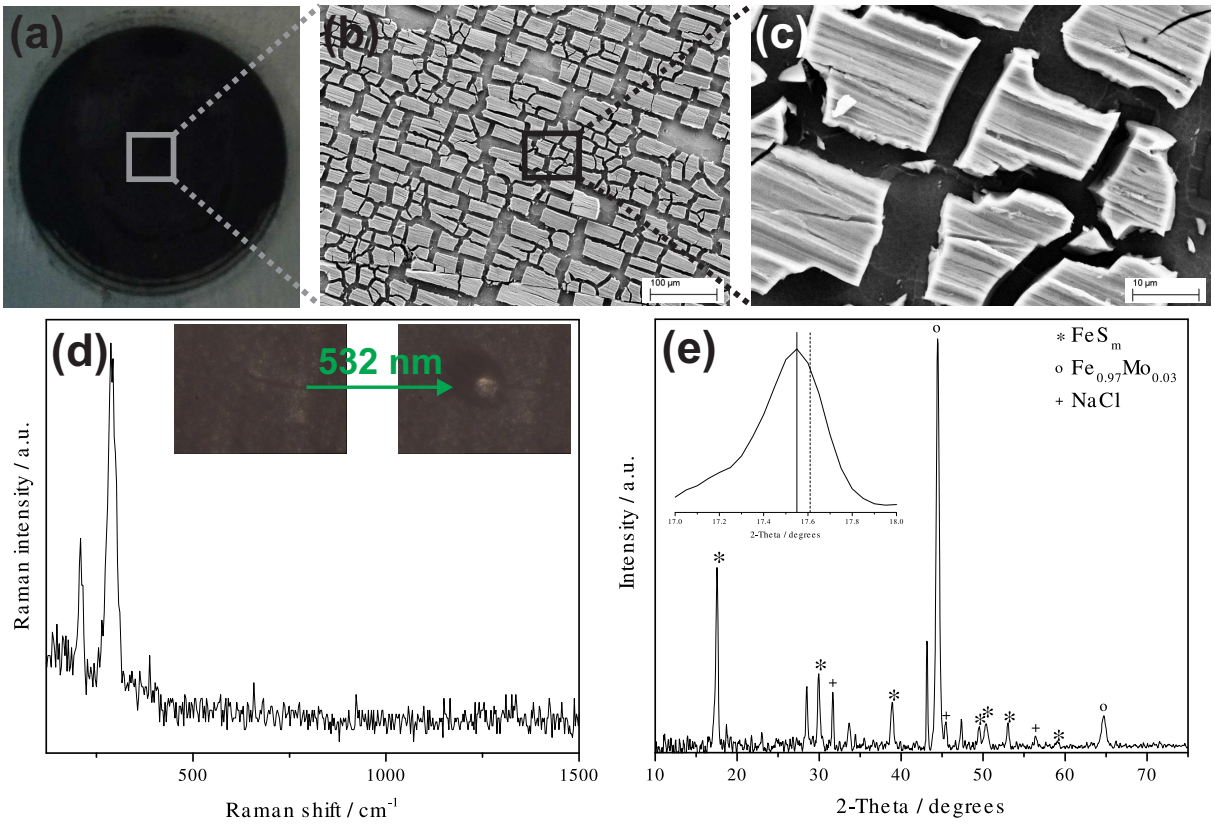

Figure 6: (a) Image of an FeMo substrate after potentiostatic polarization. (b), (c) SEM micrographs showing the morphology of the observed corrosion products. (d) Raman spectrum of the formed layer before drying (Raman band of water at ≈ 3350 cm^{-1} still present). (e) XRD pattern for the dried sample, showing the presence of mackinawite as the only crystalline corrosion product, and NaCl impurities from the electrolyte. Inset: the main 001 reflection (solid line) of mackinawite is shifted by 0.05° 2θ from the expected position (dashed line).

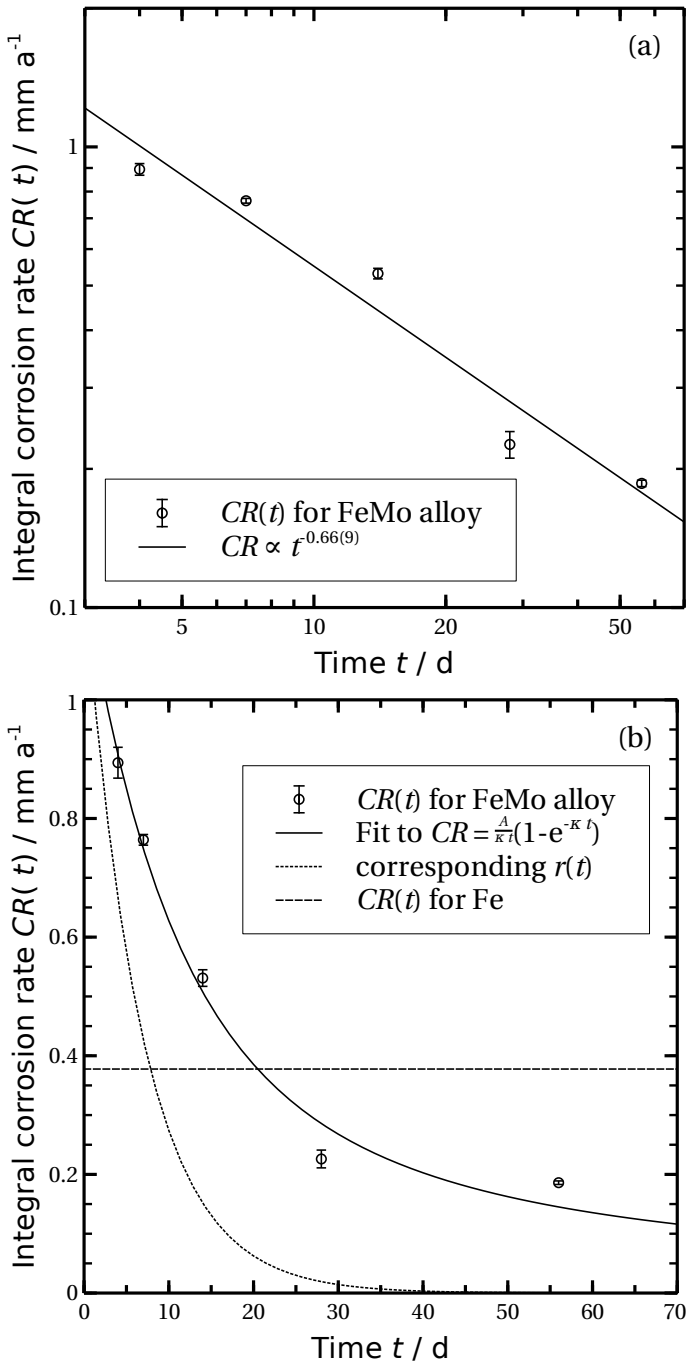

Figure 7: (a) Linear fit of FeMo $CR(t)$ on a double logarithmic scale. (b) Fit of FeMo data to eq. 3 for exponentially decaying $r(t)$. Using the parameters from the fit for $CR(t)$, the curve for $r(t)$ was calculated and is shown as dotted line. For comparison, the result of a fit of $CR(t)$ to the equation for a constant $r(t)$ to the data of pure iron is shown as dashed line.

Table 1: Electrochemical parameters extracted from LSV measurements of iron and FeMo before and after the electrochemical formation of corrosion products.

Material	β_a / V dec^{-1}	β_c / V dec^{-1}	E_{corr} / mV	i_{corr} / A cm^{-2}	R_{p} / Ω cm^2
iron	0.050	0.116	-617	4.25×10^{-5}	258
	0.025	0.072	-553	3.81×10^{-5}	172
FeMo	0.064	0.127	-598	7.61×10^{-5}	172
	0.044	0.042	-528	9.21×10^{-5}	78

Table 2: Examples of four different time dependences of instantaneous corrosion rate $r(t)$ and the integrated counterparts $CR(t)$ calculated by inserting the equations in the third column of this table into eq. 2.

	$r(t)$ is ...	$r(t) = ...$	$CR(t) = ...$	$CR(t)$ is ...
1	constant	A	A	constant
2	constant, with complete stop at time t_0	$\begin{cases} A & \forall t \leqslant t_0 \\ 0 & \forall t > t_0 \end{cases}$	$At_0/t = A'/t$	decaying with $1/t$
3	decaying with a power law	$At^{-\kappa}$	$\frac{A}{1-\kappa}t^{-\kappa} = A't^{-\kappa}$	decaying with a power law
4	decaying exponentially	$A\mathrm{e}^{-\kappa t}$	$\frac{A}{\kappa t}\left(1 - \mathrm{e}^{-\kappa t}\right)$	for large t decaying with $1/t$